Cycloidal domains in the magnetization reversal process of

$Ni_{80}Fe_{20}/Nd_{16}Co_{84}/Gd_{12}Co_{88}$ Trilayers

C. Quiros[1,2], A. Hierro-Rodriguez[3,a], A. Sorrentino[3], R. Valcarcel[3], L. M. Alvarez-Prado[1,2], J. I. Martín[1,2], J. M. Alameda[1,2], E. Pereiro[3], M. Vélez[1,2] and S. Ferrer[3]

[1]*Depto. Física, Universidad de Oviedo, 33007 Oviedo, Spain*

[2]*CINN (CSIC – Universidad de Oviedo), 33940 El Entrego, Spain*

[3]*ALBA Synchrotron, 08290 Cerdanyola del Vallès, Spain*

[a] Present address: University of Glasgow, School of Physics and Astronomy, Glasgow G12 8QQ, UK.

Abstract

The magnetization reversal of each individual layer in magnetic trilayers (Permalloy/NdCo/GdCo) has been investigated in detail with X-ray microscopy and micromagnetic calculations. Two sequential inversion mechanisms have been identified. Firstly, pairs of magnetic vortex-antivortex move along the field direction while inverting the magnetization of magnetic stripes until they are pinned by defects. The vortex-antivortex displacements are reversible within a field interval which allows their controlled motion. Second, as the reversed magnetic field increases, cycloidal domains appear in the permalloy layer as a consequence of the dissociation of vortex-antivortex pairs due to pinning. The field range where magnetic vortices and antivortices are effectively guided by the stripe pattern is of the order of tens of mT for the NiFe layer, as estimated from the stability of cycloid domains in the sample.

1. Introduction

3D magnetic textures nucleate in magnetic materials as a result of the competition of anisotropy, exchange and magnetostatic interactions. Skyrmions and helical domains occur in bulk materials with chiral exchange interactions [1,2] and also in films and nanostructures where their configuration can be tailored by confinement effects [3-5]. Non collinear textures can also be stabilized by dipolar interactions in weak perpendicular magnetic anisotropy (wPMA) materials (e.g. dipolar skyrmions in Gd/Fe [6] and dipolar merons in NdCo layers [7]) or by precessional dynamics [8]. Multilayered systems, combining materials with different exchange and anisotropy properties have been used to artificially imprint non collinear magnetic textures in soft magnetic layers (e.g. artificial skyrmions [9], meron pairs [10], vortex-antivortex pairs [11]) and, also, to stabilize non trivial spin configurations across the thickness such as topologically protected twisted magnetic helices in Dy/Fe multilayers [12].

In wPMA layers [13], the equilibrium domain pattern consists of parallel up/down stripes separated by domain walls that change from Bloch (at central plane) to Neel (top/bottom surfaces) due to stray field minimization. During in-plane magnetization reversal, Bloch points (skyrmionic number Q=1), merons (Q=1/2) and magnetic vortex-antivortex pairs (Q=1) nucleate at different sample depths and propagate guided by stripe direction [7,11,14]. In multilayers of significant thickness, stray field circulation breaks the symmetry between top/bottom sample surfaces providing a topological separation of magnetic textures in each layer [6,11]. In particular, magnetic vortex-antivortex nucleation is determined by topological characteristics (polarity, chirality and bifurcation geometry) [11,14] resulting in a robust mechanism to control the propagation of vortices and antivortices at top/bottom sample surfaces. Applications of this effect into memory devices based on the concept of magnetic vortex racetracks [15-17] would require a broad enough field range in which vortex motion can be reversibly controlled by an applied magnetic field and is effectively guided by the stripe domain pattern. These issues require a detailed characterization of the field dependent domain configuration of wPMA multilayers when vortex-antivortex pairs are present in the system.

A characteristic feature of such non-collinear spin systems is the presence of helical domains, stabilized by chiral magnetic interactions [1, 2, 18]. For thin films or in bulk materials close to sample surfaces, spin spirals can be modified by confinement effects and dipolar interactions that favor in-plane magnetization orientation [4, 5]. Then, the most stable structures are formed by the combination of helical and cycloidal domains (Figs. 1(a-b)), as it has been recently proposed and observed in chiral magnets [4, 5, 19-22]. In a simple helical domain structure, periodic along y, the magnetization rotates 2π rad in the M_x-M_z plane as sketched in Fig. 1(a). Close to an x-y sample surface, magnetostatic effects confine the 2π magnetization rotation to the M_x-M_y plane, resulting in the cycloidal domain structure, also periodic along y, sketched in
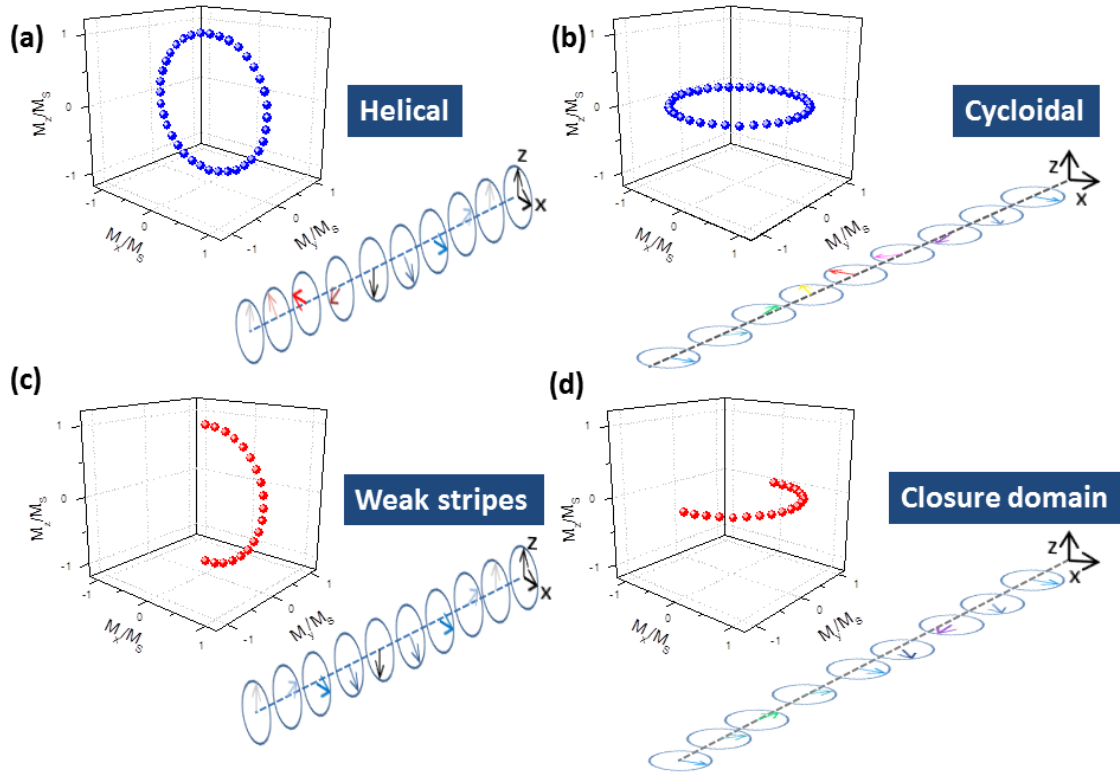

Figure 1: Sketch of spin rotation within a domain period in: (a) 2π helical domain in the M_x-M_z plane, (b) 2π cycloidal domain in the M_x-M_y plane (c) Bloch walls at the center of a weak stripe pattern (π rotation in the M_x-M_z plane from a +M_z domain to a -M_z domain through a Bloch wall with +M_x at its center) and (d) closure domains at the surfaces of a weak stripe domain pattern (π rotation in the M_x-M_y plane from a +M_y domain to a –M_y domain through a Neel wall with +M_x at its center). In all cases, the domain structures are periodic along y.

Fig. 1(b). On the contrary, weak stripe domain patterns, in the absence of chiral interactions, favor π rotations of the magnetization around the average M_x component, either in the M_x-M_z plane (inside the film) or in the M_x-M_y plane (at top/bottom film surfaces). In the first case this results in Bloch walls (Fig. 1(c)) while in the second one in closure domains at the top and bottom surfaces (Fig. 1(d)).

In this work, we report on the observation, for the first time, of cycloidal domains in soft permalloy layers using element resolved Magnetic Transmission X-ray Microscopy (MTXM). These domains are linked to the guided propagation of magnetic vortices and antivortices within the stripe domain pattern of NiFe/NdCo/GdCo trilayers. The starting point is the remanent stripe domain configuration illustrated in Fig. 2(a): the set of parallel up/down ($+M_z$/-M_z) domains in the central wPMA NdCo layer creates a closure domain pattern in both the top permalloy layer and bottom GdCo layer. The magnetization in the permalloy layer oscillates mainly in the (M_x,M_y) plane around the average $+M_x$ component (white arrow) to screen the stray field from the central NdCo layer. Upon the application of a reversed –H_x field, cycloidal domains (sketched in the M_y-M_x plane as $\rightarrow\uparrow\leftarrow\downarrow\rightarrow\uparrow$) are observed in the permalloy layer as an intermediate state between $+M_x$ ($\rightarrow\uparrow\leftarrow\uparrow\rightarrow\uparrow$ with only $+M_x$ $\uparrow$ orientation) and - M_x ($\rightarrow\downarrow\leftarrow\downarrow\rightarrow$ with only -M_x $\downarrow$) closure domains. Cycloidal domains in the Permalloy layer are stable in a field range of several tens of mT, which gives a measure of useful field range for controlled propagation of magnetic vortices and antivortices by the stripe domain pattern.

2. Experimental

Magnetic $Ni_{80}Fe_{20}$/$Nd_{16}Co_{84}$/$Gd_{12}Co_{88}$ trilayers were grown on 50 nm thick Si_3N_4 membranes by dc magnetron sputtering as reported previously [14] and characterized by Vibrating Sample (VSM) magnetometry at room temperature. Parameters for each material in
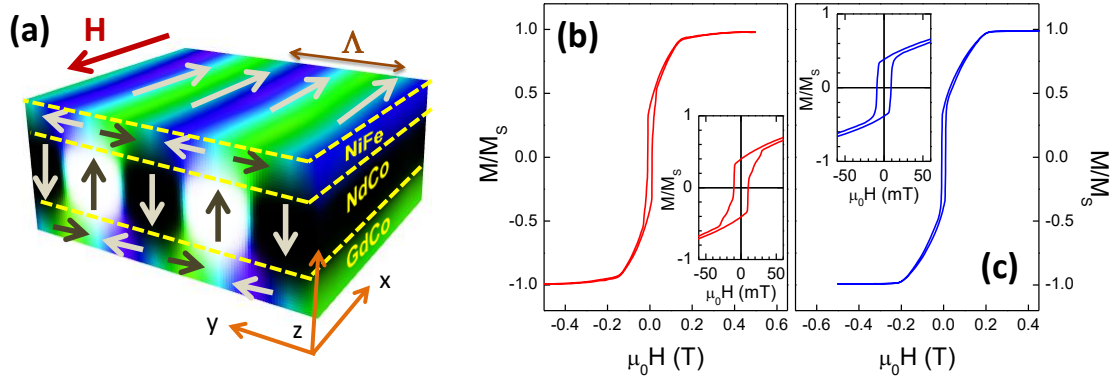
Figure 2: a) Sketch of stripe domains in a NiFe/NdCo/GdCo trilayer at remanence after saturating with $+H_x$. The stripe domain period Λ is indicated by the double arrow. b) VSM in-plane hysteresis loop of F30N40G40 trilayer. c) VSM in-plane hysteresis loop of F40N60G40 trilayer. Insets show the low field zooms of the hysteresis loops.

the trilayer were obtained from the magnetic characterization of single test layers [14]: Permalloy $Ni_{80}Fe_{20}$ has $M_S = 8.5 \times 10^5$ A/m, in plane uniaxial magnetic anisotropy $K_u = 850$ J/m^3 and a weak PMA of the order $K_N \approx 10^4$ J/m^3, induced by strains during growth but too low to induce out-of-plane domains in the samples investigated [10]; $Nd_{16}Co_{84}$ is an amorphous ferromagnetic alloy [23] with $M_S = 7 \times 10^5$ A/m and PMA $K_N \approx 10^5$ J/m^3; $Gd_{12}Co_{88}$ is a ferrimagnetic alloy with $M_S = 6 \times 10^5$ A/m and in-plane $K_u = 4.6 \times 10^3$ J/m^3 [24]. Two samples were used in this study with different layer thicknesses to check for reproducibility of the observed magnetic textures: F40N60G40 (40 nm $Ni_{80}Fe_{20}$/60 nm $Nd_{16}Co_{84}$/40 nm $Gd_{12}Co_{88}$) and F30N40G40 (30 nm $Ni_{80}Fe_{20}$/40 nm $Nd_{16}Co_{84}$/40 nm $Gd_{12}Co_{88}$). Figure 2(b-c) shows the VSM hysteresis loops of the trilayers with the applied field parallel to the sample plane. In both cases, the hysteresis loops present a transcritical shape, characterized by an almost linear decrease of in-plane magnetization from saturation (at around 200 mT) to a reduced remanence value (about 0.4 M_S), that is typical of wPMA samples with parallel stripe domain patterns (i.e. with a significant out-of-plane magnetization oscillation). The coercivity $\mu_0 H_C \approx 10$ mT is very similar in both samples (see insets in Fig. 2(b-c)), but the reversal process is broader for

F30N40G40 ($\mu_0\Delta H = 20$ mT) than for F40N60G40 ($\mu_0\Delta H = 6$ mT), indicating a stronger effect of the NdCo layer in the thinner NiFe layer of F30N40G40.

Element specific magnetic contrast images [7,14] were acquired at the transmission microscope of the Mistral Beamline at Alba synchrotron [25,26] by tuning circularly polarized X-rays to the appropriate atomic absorption energy of that element. MTXM images of the magnetization of the upper permalloy layer were acquired at the L_3 Fe absorption energy and of the bottom $Gd_{12}Co_{88}$ at the M_5 Gd absorption energy [14]. At room temperature, due to the ferrimagnetic nature of this alloy for this relative Co to rare-earth concentration, Gd magnetic moment is antiparallel to the sample magnetization which has to be taken into account in the interpretation of magnetic contrast images [24]. The X-ray angle of incidence was set at $\theta=30^{o}$ from the film normal, in order to have sensitivity to M_x and M_z magnetization components while keeping good image qualities not hindered by the decreased transmitted X ray intensities at large angles [7]. The sample was first saturated with an in-plane field $\mu_0H_x=225$ mT and imaged at remanence to establish the initial $+M_x$ magnetization state. Then, negative H_x pulses of 20 µs duration and variable amplitude were applied in-situ to monitor the magnetization reversal. The samples were imaged at remanence after each field pulse until in-plane magnetization was fully reversed.

Micromagnetic simulations of magnetization reversal were performed with the finite difference code MuMax[3] [27] in order to compare with experimental MTXM images. The trilayers were discretized into cells of dimensions of $5\times5\times3$ nm^3 for a total of 3.84×3.84 µm^2 area, using material parameters for each sublayer obtained from the magnetic characterization [13]. MuView code was used for visualization [28]. Then, the contribution to the dichroic absorption factor of each cell along the X-ray beam path was evaluated for the calculated micromagnetic configurations in order to simulate X-ray image contrasts [11].

3. Results and discussion

3.1 MTXM Hysteresis loops

Figure 3 shows several MTXM frames of a 12 x 12 μm^2 area of sample F40N60G40 imaged at the L_3 Fe edge (left panels) and M_5 Gd edge (right panels) along a sequence of reversed field pulses of increasing amplitude. Figure 3(a) shows the onset of magnetization reversal at both NiFe and GdCo layers: most of the image is covered by a pattern of bright/dark parallel stripes oriented along x direction of period Λ=175 nm. In this sample-X ray geometry [7], image contrast depends on M_x and M_z and is not sensitive to M_y: in the permalloy layer (see inset in left panel of Fig. 3(a)), white stripes correspond to $(+M_x,+M_z)$ domains and dark grey stripes to $(+M_x,-M_z)$ domains as indicated by arrows; in the GdCo layer, due to the ferrimagnetic character of the alloy, dark grey bands correspond to $(+M_x,+M_z)$ and light grey bands to $(+M_x,-M_z)$ [14]. This corresponds to a remanent domain pattern similar to the sketch in Fig. 2(a) with average in-plane magnetization orientation along $+M_x$. In Fig. 3(a), we can also observe some additional contrast levels indicating the presence of initial reversed domains (after the application of a field pulse of -22.5 mT) with a characteristic elongated shape: they typically consist of pair of reversed consecutive up/down stripes (see D1 in Fig. 3(a)) starting at a bifurcation of the stripe pattern. These domains correspond to the nucleation of a meron texture at the bifurcation core (with $Q = \frac{1}{2}$) and the propagation of Bloch points and vortex-antivortex pairs (with $Q = 1$) along the stripes direction [7,11]. At $\mu_0 H_x$=-25 mT (Fig. 3(b)), magnetization reversal has proceeded with the nucleation of new reversed domains and the propagation of existing ones: at the NiFe layer, reversed domains retain their elongated shape extending only over 1 or 2 stripe domain periods (average domain width is 1.2Λ), however, at the GdCo layer, reversed domains have grown laterally (e.g. see D2) with average domain width 4.5Λ. Finally, after a $\mu_0 H_x$=-32.5 mT pulse (Fig. 3(c)), reversal is completed in the GdCo layer whereas the magnetic configuration of the NiFe layer is highly inhomogenous. Four contrast levels can be clearly observed in the NiFe panel of Fig. 3(c): white, light gray, dark gray and black,
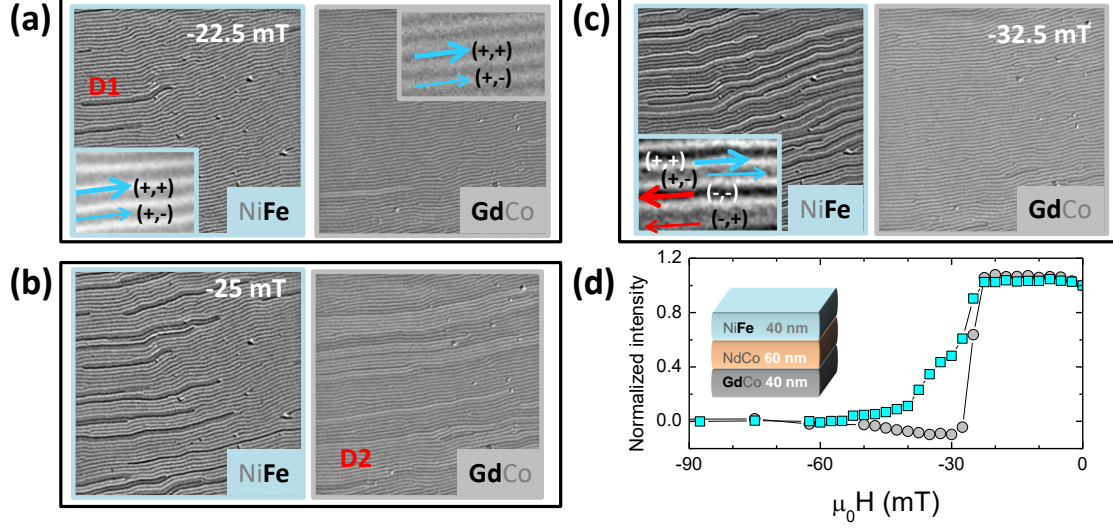
7

Figure 3: (a-c) 12 x 12 μm^2 MTXM frames of the magnetization configuration of F40N60G40 along in-plane magnetization reversal measured at L_3 Fe edge (left panels) and M_5 Gd edge (right panels). Pulsed field amplitude is indicated in each image. Insets show sketches of magnetization orientation within the stripe pattern. d) Field dependence of normalized intensity of Fe image (squares) and Gd image (circles) obtained from experimental MTXM images that allow us to reconstruct element selective hysteresis loops. Image intensities have been normalized to +1 (at remanence) and to 0 (at saturation).

corresponding to the four possible domain combinations: $(+M_x,+M_z)$, $(-M_x,+M_z)$, $(+M_x,-M_z)$ and $(-M_x,-M_z)$, respectively (see arrows in sketch) [14].

In a stripe pattern with uniform M_x sign (as the one sketched in Fig. 2), magnetic dichroic contrast oscillates in the up/down domains around a mean value given by the average M_x component [7]. Thus, we can follow in plane magnetization reversal in more detail by plotting the average image contrast as a function of reversed field amplitude (Fig. 3(d)). For both NiFe and GdCo layers, magnetization reversal starts at a similar field around -22 mT, but reversal is much easier in the GdCo layer (it is completed in $\mu_0\Delta H \approx 5$ mT) than in the NiFe layer ($\mu_0\Delta H \approx 25$ mT) indicating that expansion of reversed domains is more difficult in the NiFe layer.

Figure 4 shows a similar sequence of MTXM frames of a 12 x 12 μm^2 area of sample F30N40G40 imaged at the L_3 Fe edge (left panels) and M_5 Gd edge (right panels) along the magnetization reversal process of both NiFe and GdCo layers. Once again magnetization reversal is much easier in the GdCo than in the NiFe layer. Bottom GdCo reverses in a narrow

field interval ($\mu_0\Delta H \approx 5$ mT) by the lateral expansion of wide domains that extend over several stripe periods. Reversal at the top NiFe layer spans over $\mu_0\Delta H \approx 46$ mT, with a 12 mT plateau close to the coercivity (see Fig. 4(d)). At the initial stages of magnetization reversal in this NiFe layer ($\mu_0 H_x \approx -25$ mT, Fig. 4(a)), linear reversed domains are observed that expand along the stripe direction, as in the previous sample. Domain configuration at the plateau (-40 mT $< \mu_0 H_x$ < -28 mT) is characterized by the intermixing of stripes with opposite M_x orientation (Fig. 4(b)). Finally, $-M_x$ domains extending over several stripe domain periods appear in the image for $\mu_0 H_x$ < -40 mT (Fig. 4(c)). NiFe layer reversal is completed at $\mu_0 H_x \approx -60$ mT.

Thus, in both samples the field interval for magnetization reversal in the Permalloy layer is significantly broader than in the GdCo layer (by a factor of 5 -10), which might seem surprising in view of the softer magnetic behavior of simple permalloy layers. It suggests a crucial role of the stripe pattern imprinted by the NdCo central layer in the propagation of reversed domains in the top/bottom layers that requires a careful analysis of the MTXM images.
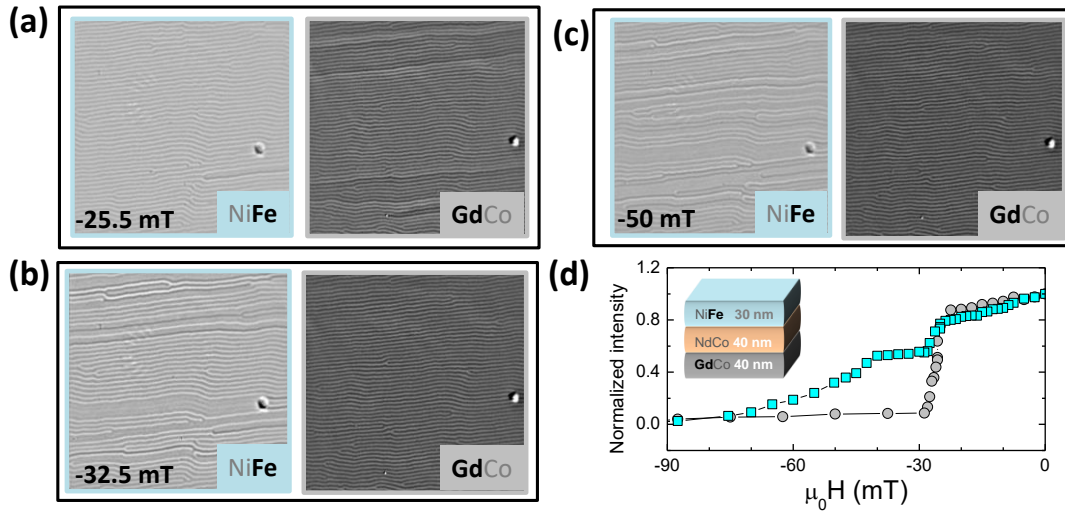

Figure 4: (a-c) 12 x 12 μm^2 MTXM frames of the magnetization configuration of F30N40G40 along in-plane magnetization reversal measured at L_3 Fe edge (left panels) and M_5 Gd edge (right panels). Pulsed field amplitude is indicated in each image. In this case, M_5 Gd edge images were acquired along the ascending branch of the hysteresis loop at positive fields of the same amplitude as indicated in each panel. d) Field dependence of normalized intensity of Fe image (squares) and Gd image (circles) obtained from experimental MTXM images that allow us to reconstruct the element selective hysteresis loop.

3.2 Reversible domain expansion at the onset of magnetization reversal

Figure 5 shows a detail of domain propagation at the onset of magnetization reversal in the bottom GdCo layer of F30N40G40, driven by a sequence of positive/negative field pulses. At the initial state (Fig. 5(a)), we can see the boundary between a $-M_x$ domain (lower part of the image) and a $+M_x$ domain (upper part of the image) that runs along a dark grey $(-M_x,+M_z)$/black $(+M_x,+M_z)$ stripe (see dotted line in Fig. 5(a)). It has been recently shown [11] that, due to geometrical restrictions by stray field circulation and the periodicity of the stripe pattern, the magnetic texture that separates the dark grey $(-M_x,+M_z)$ and the black $(+M_x,+M_z)$ stripe portions at the bottom sample surface consists of a magnetic vortex with $+M_z$ polarity as inferred from micromagnetic simulations (see inset of Fig. 5(a)).

In the experiment depicted in Fig. 5, we observe the propagation of this magnetic vortex along the $+M_z$ stripe (dashed vertical lines in Fig. 5(a)), using as a reference the position of Y_1, the black bifurcation at the left of each panel (vertical solid line in Fig. 5(a)). Also, in Fig 5a, the separation between bifurcations Y_1 and Y_2 is 4 μm that we denote as X_{max}. Fig. 5(b) summarizes the results after applying successive field pulses. First, a set of equal amplitude 7.5 mT pulses drove the vortex slowly to the right (increasing X in the upper panel), until it stopped at the intermediate position $X \approx 0.3\ X_{max}$. Increasing pulse amplitudes up to 12 mT, depinned the vortex from this intermediate position and pushed it up to bifurcation Y_2 (the endpoint of this black stripe). Then, a set of negative field pulses of increasing amplitude was applied to the sample. No changes in the image were detected until the vortex jumped back to $X \approx 0.2\ X_{max}$ after a -14 mT pulse. The remaining pulse sequence showed a reversible motion of the vortex along the stripe from $0.2X_{max}$ to X_{max}, depending on pulse amplitude and sign. It is important to mention here that the position of bifurcations Y_1 and Y_2 is not altered by the field pulses applied for the present experiment.
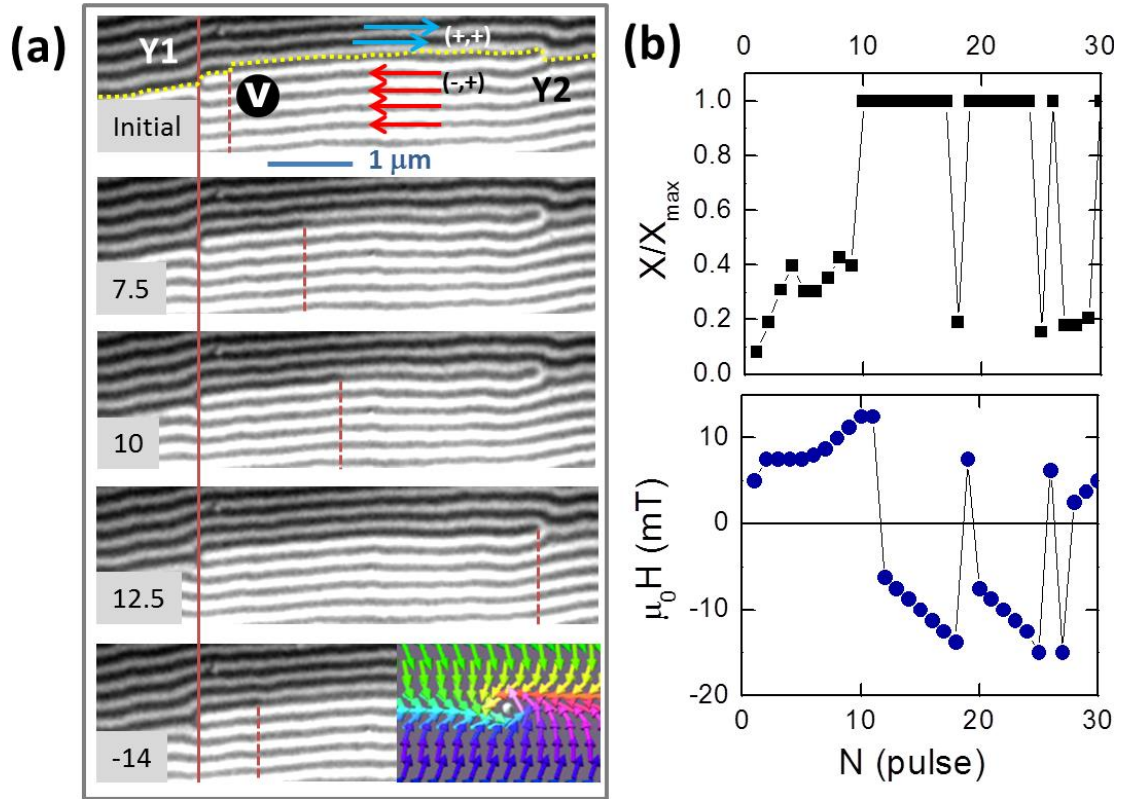
Figure 5: a) Detail of MTXM images at M_5 Gd edge of F30N40G40 under a sequence of positive/negative field pulses (field in mT indicated in left corner of each panel). Arrows indicate magnetization orientation in black $(+M_x,+M_z)$ and dark gray $(-M_x, +M_z)$ stripes. Horizontal dotted line indicates the initial boundary between $+M_x$ and $-M_x$ domains and vertical dashed lines indicate vortex position (i.e. limit between black $(+M_x,+M_z)$ and dark gray $(-M_x,+M_z)$ regions in the central stripe). Inset at lowest panel is a micromagnetic simulation of a vortex propagating along a $+M_z$ stripe at the GdCo bottom surface. b) Vortex displacement (top panel) and field sequence (bottom panel) showing reversible motion within range. Vortex displacement is in units of $X_{max} = 4$ μm, the distance between bifurcations Y_1 and Y_2.

In our previous works [11,14], bifurcations within the stripe pattern were identified as nucleation sites for reversed M_x domains that expanded away from the bifurcation by the propagation of vortices and antivortices along the stripes direction. This mechanism gives rise to elongated domains of width Λ similar to D1 in Fig. 3(a). Now, the experiment described in Fig. 5, evidences an additional role of bifurcations as pinning sites: as a vortex and/or antivortex reaches a stripe endpoint, further expansion of the reversed domain is hindered. Thus, additional mechanisms must come into play to complete the magnetization reversal of the sample.

3.3 Closure and cycloidal domains at coercivity

As the magnetization reversal process proceeds within the NiFe and GdCo layers, four types of in-plane domains can be identified by comparing experimental MTXM Fe edge images (Fig. 6(a)) with simulated contrast images derived from micromagnetic simulations (Fig. 6(b)) using the formalism described in ref. [11]. These four domain types are: i) initial $+M_x$ domains characterized by alternating $(+M_x,+M_z)$ and $(+M_x,-M_z)$ stripes, i.e. alternating white/dark gray bands; ii) partially reversed domains with alternating $(+M_x,-M_z)$ and $(-M_x,+M_z)$ stripes, i.e. alternating dark gray/light gray bands; iii) partially reversed domains with alternating $(+M_x,+M_z)$ and $(-M_x,-M_z)$ stripes, i.e. alternating white/black bands; iv) fully reversed $-M_x$ domains with alternating $(-M_x,+M_z)$ and $(-M_x,-M_z)$ stripes, i.e. alternating light gray/black bands. Figure 6 (a-c) displays from top to bottom these fourth domain types. The local sense of M_y in between stripes is not directly accessible experimentally at the measurement configuration
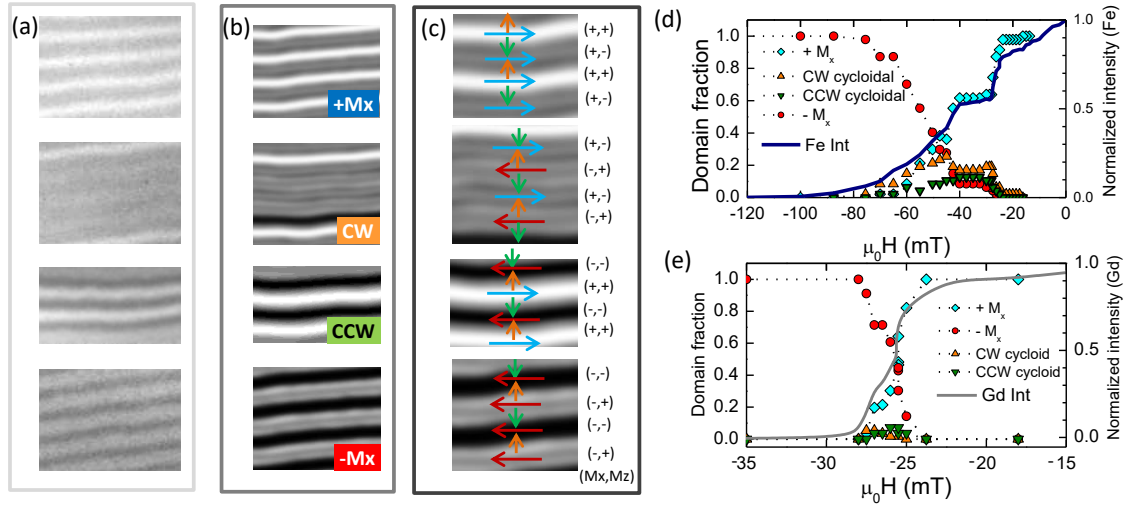

Figure 6: (a) Four domain types at NiFe layer (selected from MTXM images of F30N40G40); (b) Simulated MTXM contrast from micromagnetic simulations in different domain configurations; (c) Sketch of in-plane magnetization orientation at each contrast level (making a zoom of the central regions of panels in (b) for the sake of clarity in the arrow sketches); (d-e) Fraction of each domain type vs. reverse field amplitude at NiFe layer (d) and GdCo layer (e). Field dependence of average image contrast at each layer is also shown for comparison (solid line).

(only sensitive to M_x and M_z components). However, it can be uniquely determined by the sense of circulation of stray field at the top sample surface (coming out of the sample at $+M_z$ stripes and entering it at $–M_z$ stripes). This allows us to draw the M_x-M_y sketches for each domain type, shown in Fig. 6(c), which are confirmed by micromagnetic simulations. Thus, partially reversed domains ii) and iii) are identified as cycloidal domains with opposite rotation senses.

The fraction of each domain type along the magnetization reversal process is shown in Figs. 6(d-e) for the NiFe and GdCo layers. At the onset of reversal, the sample is covered by $+M_x$ domains, that disappear gradually along the reversal process, with a field dependence very similar to the average intensity in each layer (see solid lines in Figs. 6(d-e)). Fully reversed $-M_x$ domains follow the opposite trend, appearing at the onset of magnetization reversal and covering the sample at saturation at both top and bottom layers. However, the prevalence of cycloidal domains is very different at NiFe and GdCo. In the NiFe case a significant fraction of cycloidal domains appears (covering up to 30% of the sample) with a wide stability range from -22 mT down to -70 mT. At the GdCo layer, the fraction of cycloidal domains barely reaches a 5%, localized mainly at the boundary between $+M_x$ and $–M_x$ domains. Thus, the stability of cycloidal domains at the soft NiFe layer appears as the direct cause of the slower reversal process in this layer, making it a suitable material for the controlled propagation of vortex-antivortex pairs in a broad enough field interval.

The stability of cycloidal domains in NiFe and GdCo is related with topological restrictions in the stripe pattern of the central NdCo layer, imprinted by exchange and magnetostatic interactions at the top/bottom layers. Then, it is interesting to note that the best stability range (broadest plateau in the magnetization reversal process) is found for the NiFe layer of F30N40G40 (i.e. the thinnest layer with smallest in-plane anisotropy), as observed both in the macroscopic hysteresis loops (Fig. 2) and in MTXM loops (Figs. 3 and 4). This could be related with the large exchange contribution of cycloidal domains (with 2π magnetization rotations on a small length scale), that scales with NiFe layer thickness favoring their observation in thin

magnetic layers. In a similar way, the higher in-plane anisotropy of GdCo would increase the anisotropy contribution in a cycloidal domain configuration, reducing their stability and the effective field range for controlled propagation of vortex-antivortex pairs.

3.4 Micromagnetic simulations

Figure 7(a) shows the field dependence of the magnetization during an in-plane reversal process at each layer obtained from micromagnetic simulations of the F40N60G40 trilayer that qualitatively reproduces the experimental behavior. As the field is reduced from saturation (see inset at Fig. 7(a)) in plane M_x is reduced in each layer due to the development of the stripe domain pattern with a significant M_z oscillation. At remanence M_x is lowest at the central NdCo layer (M_R(NdCo)= 0.2 M_S) but retains relatively large values at the top NiFe (M_R(NiFe)= 0.6 M_S) and bottom GdCo (M_R(GdCo)= 0.5 M_S) where the closure domain structures are localized. For negative fields, reversed domains nucleate at stripe bifurcations and propagate by the correlated motion of vortex-antivortex pairs, as shown in Fig. 7(b1). These initial reversed domains are only one stripe period wide (Λ), similar to those observed in Figs. 3(a) and 4(a). This process starts at -4 mT at GdCo and -8 mT at NdCo and NiFe and results in a steep decrease of the magnetization down to coercivity ($M_x \approx 0$).

Depending on bifurcation arrangement in each layer, the vortex-antivortex pair can be dissociated, as shown in Fig. 7(b2) where the antivortex is pinned by interaction with a bifurcation and the vortex has propagated further. In the region between the vortex and the antivortex the magnetization adopts a cycloidal configuration with alternating $+M_x$ and $-M_x$ stripes. Individual vortex propagation (uncoupled from its corresponding antivortex) was observed in the experiment of Fig. 5, and is also seen in the NiFe images of Figs. 3(b-c) and 4(b-c) i.e. in the field range where cycloidal domains appear in the sample.

As the negative field increases, vortices and antivortices propagate guided by the stripes direction until they are stopped by stripe endpoints (as shown in Fig. 7(b3)). At the simulated sample, the number of bifurcations is relatively small (between 4 and 6), so that a stable

magnetization configuration with all vortices pinned at stripe endpoints is easily reached both for the NiFe and GdCo layers. It results in a magnetization plateau just below coercivity that extends over a $\Delta\mu_0 H = 6$ mT interval at GdCo and over $\Delta\mu_0 H = 14$ mT at NiFe layer.

Finally, a steep decrease of M_x is observed starting at -20 mT for GdCo and at -28 mT at NiFe layer. It corresponds to the activation of an additional magnetization reversal mechanism by the propagation of a domain wall in the x-z plane along the y direction, i.e. perpendicular to the direction of the stripes (see Figs. 7(b4-b5)), indicating that vortex-antivortex propagation has ceased to be confined along the stripes. At this point of the hysteresis loop, the sample surface is fully covered by $-M_x$ domains. The remaining part of the reversal process corresponds to the approach to $-M_x$ saturation as the amplitude of the M_z oscillation in the stripe pattern is reduced for large negative H_x fields.
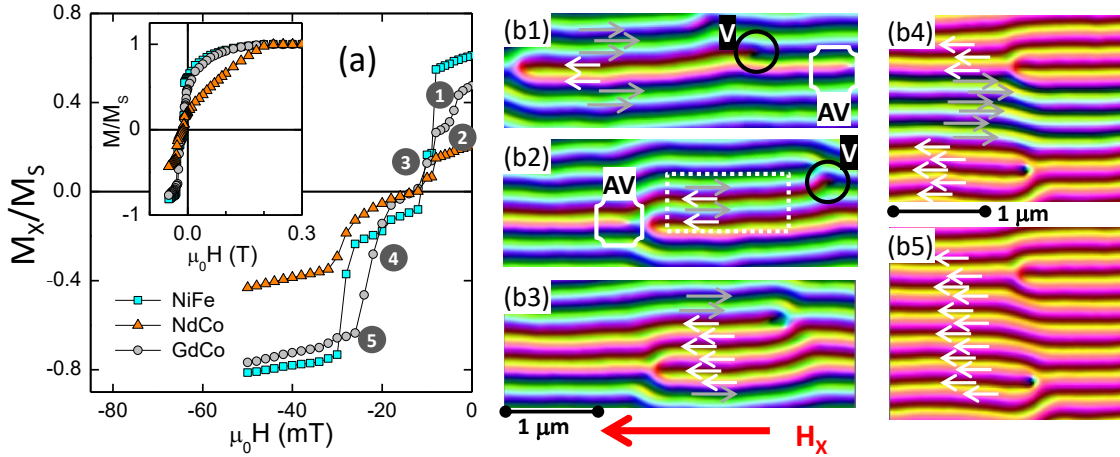

Figure 7: a) Element resolved hysteresis loop, calculated by micromagnetic simulations at F40N60G40. Numbers correspond to images in panel (b). b) Magnetic configuration of GdCo layer showing V-AV propagation parallel to stripes direction at onset of magnetization reversal: (b1) -4 mT, (b2) -6 mT, (b3) -9 mT ((b2) and (b3) are displaced to the right relative to (b1) to keep track of the propagating vortex-antivortex pair), and domain wall propagation perpendicular to stripes at the last part of the magnetization reversal: (b4) -24 mT, (b5) -26 mT. Arrows indicate M_x sense in each stripe. Note the cycloidal domain in (b2) due to pinning of an antivortex at the bifurcation, highlighted by the dotted rectangle. Also, a certain displacement of bifurcations along the stripes directions can be observed between (b2) and (b3).

Spin rotations in the simulated closure domain patterns can be seen in more detail in Fig. 8. $+M_x$ closure domains (circles in Fig. 8(a) and sketch of Fig. 8(b) combine an in-plane (M_x-M_y) π rotation correlated with a M_z oscillation of reduced amplitude $\pm0.5M_S$, so that the magnetization is always constrained to the $+M_x$ hemisphere. The configuration of $-M_x$ closure domains is equivalent but with magnetization in the $-M_x$ hemisphere (squares in Fig. 8(a) and sketch of Fig. 8(d)). Partially reversed domains are a combination of an in-plane cycloid (2π rotation in the M_x-M_y plane rotation) with a correlated M_z oscillation (triangles in Fig. 8(a) and sketch of Fig. 8(c)). Two possible rotation senses can appear depending on the relative phase between the in-plane and out-of-plane spin rotations, as observed experimentally.
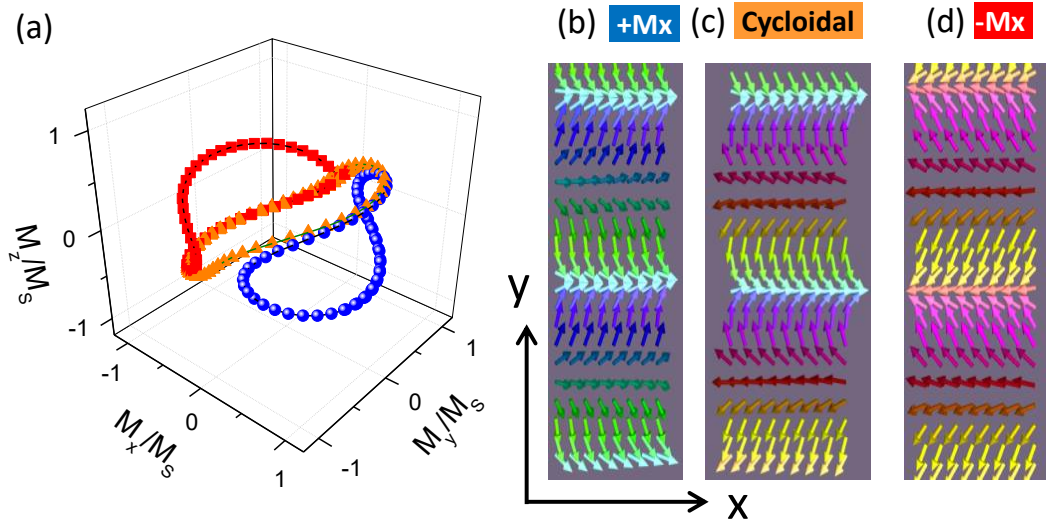

Figure 8: (a) Spin rotation at the bottom GdCo, derived from the micromagnetic simulations in Fig. 7: blue circles, $+M_x$ domain; orange triangles, cycloidal; red squares, $-M_x$ domain. The corresponding magnetic configurations are shown in (b), (c) and (d).

The comparison between micromagnetic simulations and the experimental MTXM images shows that the observation of partially reversed cycloidal domains requires two basic ingredients: 1) Effective vortex/antivortex guiding along the stripe domain pattern, i.e. that the propagation of domain walls transverse to the stripes is delayed to high enough magnetic fields. 2) The dissociation of vortex-antivortex pairs as they propagate along the stripe pattern. This can occur by interaction with stripe bifurcations (as seen in Fig. 7(b2)) or other defects present

in the sample (as seen in experimental images of Figs. 3-4). Experimentally, these conditions are clearly met only at the NiFe layer but not at the GdCo layer.

Thus the observation of cycloidal domains in the experimental MTXM images can be used to characterize the field range where vortices and antivortices are effectively guided by the stripe pattern, which is of the order of tens of mT for the NiFe layer. This is an interesting result since the existence of a broad enough field interval of effective vortex guiding is essential for possible applications of the deterministic propagation of vortex-antivortex pairs found in ref. [11].

4. Conclusions

In summary, cycloidal domains have been identified in NiFe layers during the magnetization reversal process of NiFe/NdCo/GdCo trilayers by the comparison of MTXM images and micromagnetic simulations. The stripe pattern of the central wPMA NdCo layer imprints a periodic closure domain structure at the top/bottom NiFe and GdCo layers where magnetization reversal is initiated at stripe bifurcations, by the nucleation of vortex-antivortex pairs. It is found that, in the NiFe layer, there is a field range around coercivity (of several tens of mT) in which pairs of vortices and antivortices propagate preferentially along the stripes and, then, they dissociate while pinning at stripe endpoints and sample imperfections. The sensitivity of MTXM images to M_z and M_x components at the different layers has revealed that, at that point of the hysteresis loop, cycloidal domains with alternating M_x sign appear in the sample, covering up to 30% of the NiFe surface. The stability range of cycloidal domains gives a measure of the field interval in which propagation of vortices and antivortices within the NiFe layer can be effectively controlled by the stripe pattern.

References

[1] U. K. Rößler, A. N. Bogdanov, and C. Pfleiderer, *Spontaneous skyrmion ground states in magnetic metals*, Nature **442**, 797 (2006).

[2] X. Yu, M. Mostovoy, Y. Tokunaga, W. Zhang, K. Kimoto, Y. Matsui, Y. Kaneko, N. Nagaosa, and Y. Tokura, *Magnetic stripes and skyrmions with helicity reversals*, PNAS **109**, 8856 (2012).

[3] F. Zheng, H. Li, S. Wang, D. Song, C. Jin, W. Wei, A. Kovács, J. Zang, M. Tian, Y. Zhang, H. Du, and R. E. Dunin-Borkowski, *Direct Imaging of a Zero-Field Target Skyrmion and Its Polarity Switch in a Chiral Magnetic Nanodisk*, Phys. Rev. Lett. **119**, 197205 (2017).

[4] F. N. Rybakov, A. B. Borisov, S. Blügel and N. S. Kiselev, *New spiral state and skyrmion lattice in 3D model of chiral magnets*, New J. Phys. **18**, 045002 (2016).

[5] L. Schmidt, J. Hagemeister, P.-J. Hsu, A. Kubetzka, K. von Bergmann and R. Wiesendanger, *Symmetry breaking in spin spirals and skyrmions by in-plane and canted magnetic fields*, New J. Phys. **18**, 075007(2016).

[6] S. A. Montoya, S. Couture, J. J. Chess, J. C. T. Lee, N. Kent, D. Henze, S. K. Sinha, M.-Y. Im, S. D. Kevan, P. Fischer, B. J. McMorran, V. Lomakin, S. Roy, and E. E. Fullerton, *Tailoring magnetic energies to form dipole skyrmions and skyrmion lattices*, Phys. Rev. B **95**, 024415 (2017).

[7] C. Blanco-Roldán, C. Quirós, A. Sorrentino, A. Hierro-Rodríguez, L. M. Álvarez Prado, R. Valcárcel, M. Duch, N. Torras, J. Esteve, J. I. Martín, M. Vélez, J. M. Alameda, E. Pereiro, and S. Ferrer, *Nanoscale imaging of buried topological defects with quantitative X-ray magnetic microscopy*, Nature Comm. **6**, 8196 (2015).

[8] Y. Zhou, E. Iacocca, A. A. Awad, R. K. Dumas, F. C. Zhang, H. B. Braun & J. Åkerman, *Dynamically stabilized magnetic skyrmions*, Nature Comm. **6**, 8193 (2015).

[9] J. Li, K. W. Moon, A. Doran, M. A. Marcus, A. T. Young, E. Arenholz, S. Ma, R. F. Yang, C. Hwang and Z. Q. Qiu, *Tailoring the topology of an artificial magnetic skyrmion*, Nature Comm. **5**, 4704 (2014).

[10] S. Wintz, C. Bunce, A. Neudert, M. Körner, T. Strache, M. Buhl, A. Erbe, S. Gemming, J. Raabe, C. Quitmann, and J. Fassbender, *Topology and Origin of Effective Spin Meron Pairs in Ferromagnetic Multilayer Elements*, Phys. Rev. Lett. **110**, 177201 (2013).

[11] A. Hierro-Rodriguez, C. Quirós, A. Sorrentino, R. Valcárcel, I. Estébanez, L. M. Alvarez-Prado, J. I. Martín, J. M. Alameda, E. Pereiro, M. Vélez, and S. Ferrer, *Deterministic propagation of vortex-antivortex pairs in magnetic trilayers*, Appl. Phys. Lett. **110**, 262402 (2017).

[12] S. Fust, S. Mukherjee, N. Paul, J. Stahn, W. Kreuzpaintner, P. Böni and A. Paul, *Realizing topological stability of magnetic helices in exchange-coupled multilayers for all-spin-based system*, Sci. Rep. **6**, 19315 (2016).

[13] A. Hubert and R. Schäfer. *Magnetic Domains: The Analysis of Magnetic Nanostructures* (Springer, 1998).

[14] A. Hierro-Rodriguez, C. Quirós, A. Sorrentino, C. Blanco-Roldán, L. M. Alvarez-Prado, J. I. Martín, J. M. Alameda, E. Pereiro, M. Vélez, and S. Ferrer, *Observation of asymmetric distributions of magnetic singularities across magnetic multilayers*, Phys. Rev. B **95**, 014430 (2017).

[15] M. Manfrini, Joo-Von Kim, S. Petit-Watelot, W. Van Roy, L. Lagae, C. Chappert and T. Devolder, *Propagation of magnetic vortices using nanocontacts as tunable attractors*, Nature Nanotech. **9**, 121 (2014).

[16] S. Zhang, A. A. Baker, S. Komineas and T. Hesjedal, *Topological computation based on direct magnetic logic communication*, Sci. Rep. **5**, 15773 (2015).

[17] L. D. Geng and Y. M. Yin, *Magnetic vortex racetrack memory*, J. Magn. Magn. Mater. **423**, 84 (2017).

[18] F. Li, T. Nattermann, and V. L. Pokrovsky, *Vortex Domain Walls in Helical Magnets*, Phys. Rev. Lett. **108**, 107203 (2012).

[19] S. Meckler, N. Mikuszeit, A. Preßler, E.Y. Vedmedenko, O. Pietzsch, and R. Wiesendanger, *Real-Space Observation of a Right-Rotating Inhomogeneous Cycloidal Spin Spiral by Spin-Polarized Scanning Tunneling Microscopy in a Triple Axes Vector Magnet*, Phys. Rev. Lett. **103**, 157201 (2009).

[20] M. Haze, Y. Yoshida and Y. Hasegawa, *Experimental verification of the rotational type of chiral spin spiral structures by spin-polarized scanning tunneling microscopy*, Sci. Rep. **7**, 13269 (2017).

[21] I. Gross, W. Akhtar, V. Garcia, L. J. Martínez, S. Chouaieb, K. Garcia, C. Carretero, A. Barthélémy, P. Appel, P. Maletinsky, J.-V. Kim, J. Y. Chauleau, N. Jaouen, M. Viret, M. Bibes, S. Fusil and V. Jacques, *Real-space imaging of non-collinear antiferromagnetic order with a single-spin magnetometer*, Nature **549**, 252 (2017).

[22] N. Mikuszeit, S. Meckler, R. Wiesendanger, and R. Miranda, *Magnetostatics and the rotational sense of cycloidal spin spirals*, Phys. Rev. B **84**, 054404 (2011).

[23] A. Hierro-Rodriguez, R. Cid, M. Vélez, G. Rodriguez-Rodriguez, J. I. Martín, L. M. Alvarez- Prado, J. M. Alameda, *Topological Defects and Misfit Strain in Magnetic Stripe Domains of Lateral Multilayers With Perpendicular Magnetic Anisotropy*, Phys. Rev. Lett. **109**, 117202 (2012).

[24] C. Blanco-Roldán, Y. Choi, C. Quirós, S. M. Valvidares, R. Zarate, M. Vélez, J. M. Alameda, D. Haskel, and J. I. Martín, *Tuning interfacial domain walls in GdCo/Gd/GdCo' spring magnets*, Phys. Rev. B **92**, 224433 (2015).

[25] E. Pereiro, J. Nicolas, S. Ferrer, and M. R. Howells, *A soft X-ray beamline for transmission X-ray microscopy at ALBA*, J. Synchrotron Rad. **16**, 505 (2009).

[26] A. Sorrentino, J. Nicolás, R. Valcárcel, F. J. Chichón, M. Rosanes, J. Avila, A. Tkachuk, J. Irwin, S. Ferrer and E. Pereiro, *MISTRAL: a transmission soft X-ray microscopy beamline for cryo nano-tomography of biological samples and magnetic domains imaging*, J. Synchrotron Rad. **22**, 1112 (2015).

[27] A. Vansteenkiste, J. Leliaert, M. Dvornik, M. Helsen, F. Garcia-Sanchez and B. Van Waeyenberge, *The design and verification of MuMax3*, AIP Advances **4**, 107133 (2014).

[28] G. E. Rowland, *Muview*, http://www.grahamerowlands.com/main/muview